Breakup of a Drop in a Liquid–Liquid Pipe Flow through an Orifice

S. Galinat, L. Garrido Torres, and O. Masbernat
Laboratoire de Génie Chimique UMR 5503 CNRS/INPT/UPS, BP 1301, 31106 Toulouse cedex 1, France

P. Guiraud
Laboratoire d'Ingénierie des Procédés de l'Environnement, INSA Toulouse, F-31077 Toulouse cedex 4, France

F. Risso
Institut de Mécanique des Fluides de Toulouse, UMR 5502 CNRS/INPT/UPS, 31400 Toulouse, France

C. Dalmazzone and C. Noik
Institut Français du Pétrole, Division Chimie et Physico-Chimie Appliquées, 92852 Rueil-Malmaison Cedex, France

DOI 10.1002/aic.11055
Published online November 27, 2006 in Wiley InterScience (www.interscience.wiley.com).

The drop breakup in a heterogeneous turbulent pipe flow developing downstream of an orifice is reported. A two-phase flow is considered of n-heptane drops in a water–glycerin solution at three distinct volume concentrations: $\phi_d = 0$ (single-phase flow), 0.1, and 0.2. The maximum pressure drop across the orifice, ΔP_{max}, is found to be a linear function of the kinetic energy of the mixture that weakly depends on ϕ_d. The continuous-phase velocity field is measured by means of high-speed particle image velocimetry in an optically homogeneous medium. The turbulence energy level and its spatial distribution are strongly influenced by both the continuous-phase viscosity and the presence of the dispersed phase. Drop breakup is driven by an inertial mechanism and is observed where the turbulence is the most intense. The breakup probability, the mean number of fragments, and the daughter-drop Sauter diameter are plotted against the global Weber number based on ΔP_{max}. For concentrations up to 0.1, breakup statistics are close to those obtained with an isolated drop in a single-phase flow of water. For $\phi_d = 0.2$, the increase of breakup probability with the Weber number becomes weaker because of the volume reduction of the region of intense turbulence. The evolution of breakup probability with the distance from the orifice indeed shows strong differences between the test cases, arising from modifications in the local structure of the heterogeneous turbulence field. © 2006 American Institute of Chemical Engineers *AIChE J,* 53: 56–68, 2007

Keywords: drop breakup, two-phase dispersed flow, heterogeneous turbulence, breakup probability

Introduction

Despite the large number of applications concerned, breakup of drops in liquid–liquid dispersions remains an open problem that requires considerable efforts to collect accurate data and propose relevant models. In many practical situations (stirred vessels, columns, or pipe flows) the dispersed flow is turbulent, spatially heterogeneous, and involves a concentrated dispersed phase. In these complex situations, experimental studies are often limited to global approaches, that is, which do not consider the micro-hydrodynamics at the scale of the drop. As a consequence, the proposed scaling laws are valid only for the particular flow generated in the device under consideration. It is therefore necessary to combine the local analysis of both the flow structure and

Correspondence concerning this article should be addressed to O. Masbernat at olivier.masbernat@ensiacet.fr.

breakup mechanism to derive models with a significantly broad range of validity.[1] For concentrated dispersions, the complexity of the problem is further increased as a consequence of the hydrodynamic interactions between the carrier flow and the drops, even in the absence of coalescence or polydispersity.

Most of the investigations of the role of the concentration on the breakup of drops were carried out in stirred vessels. For a given impeller rotation speed, increasing the dispersed phase concentration generally leads to the formation of larger drops.[2–4] Correlations for the mean diameter based on the Hinze–Kolmogorov theory were derived in the limit of dilute dispersions, some of them accounting for the viscous dissipation inside the drop during the breakage process.[5] The mean diameter was modeled with increasing power laws of the concentration.[6–8] The effect of the turbulence modulation by the dispersed phase was considered by Kumar et al.[9] for systems with a low coalescence rate and concentration < 0.4. For $\phi > 0.5$, these authors observed a decrease of the drop diameter, a phenomenon they attributed to the predominance of a capillary breakup mechanism induced by the elongational flow in between the impeller blades. However, because of the lack of experimental data on the local flow field in concentrated systems, this interpretation is not demonstrated and the effect of the dispersed phase concentration on the resulting drop size is not yet elucidated. More recently, an experimental study considering concentrations up to 0.6 showed that the classical 5/3 power law relating the Weber number to the drop size was not verified in concentrated dispersions, the exponent being found to become a decreasing function of ϕ.[10] At high concentrations, a better knowledge of the effect of the dispersed-phase concentration on the turbulent flow surrounding the drops is therefore necessary.

Highly concentrated dispersions are commonly encountered in oil recovery processes, which involve the transport of water-in-oil emulsions in pipes under turbulent flow conditions. The knowledge of the drop size distribution within the dispersion is an important issue with respect to the ultimate phase separation. The various breakup events occurring in the duct need to be modeled, especially at the crossing of singularities (pipe restrictions or enlargement, elbows), which are generally associated with high rates of energy dissipation. In a previous study,[11] we investigated the fragmentation of an isolated drop of *n*-heptane downstream of a concentric orifice in a vertical pipe flow of water. In the range of Reynolds numbers and restriction ratios investigated, the breakup probability, the mean number of fragments, and the resulting drop size distribution were found to be controlled by a unique dimensionless group, the global Weber number:

$$\mathrm{We} = \frac{\Delta P_{\max} d}{\sigma} \tag{1}$$

where $\Delta P_{\max}$ is the maximum pressure drop across the orifice, d is the initial drop diameter, and σ is the interfacial tension. In particular, the breakup probability was found to be a monotonic increasing function of We. The present work addresses the role of the dispersed-phase concentration. In the same experimental setup, the breakup process in a concentrated dispersion of *n*-heptane drops in a water–glycerin solution is now studied. To analyze the breakup mechanism, a detailed description of the velocity field of the carrier fluid is provided and the breakup statistics in concentrated dispersions are compared with those obtained with an isolated drop in two single-phase flows of different continuous-phase viscosities. By this way, one can expect to disentangle the effect of concentration from that of the viscosity of the two-phase mixture.

The article is structured as follows: the experimental setup, characteristics of the test cases, and measurement techniques are presented in section 2. Section 3 presents the local measurements of the velocity field downstream of the orifice for two single-phase flows of different viscosities and for two two-phase flows of concentrations $\phi_d = 0.1$ and 0.2. The measurements are obtained by means of high-speed particle image velocimetry (PIV), the two-phase mixture being made transparent as the result of optical index matching of the continuous and dispersed phases. In section 4, the motion, deformation, and breakup of individual colored drops are obtained by means of high-speed video. The probability of breakup, the mean number of fragments, and the daughter-drop mean diameter are presented for both single- and two-phase flow configurations. In section 5, the roles of the continuous-phase viscosity and that of the mixture concentration on breakup mechanism are analyzed, based on the knowledge of breakup statistics and local hydrodynamics. Main results of this study are summarized in the last section.

Experimental Setup and Instrumentation

The liquid–liquid flow loop

The flow loop used in this study (Figure 1) was described in detail in Galinat et al.[11] It consists of a 1-m high vertical Altuglas® pipe (Altuglas International, Philadelphia, PA) of internal diameter $D = 30$ mm, equipped with a circular concentric orifice. At the duct bottom, the continuous phase is fed by a stainless steel convergent section. For the study of isolated drops, a capillary tube with an inner diameter of 0.6 mm is mounted perpendicularly to the duct wall. Heptane drops with a diameter d ranging between 1.5 and 3 mm are injected by an electric syringe pump. For two-phase flow configurations, a narrow size distribution population of *n*-heptane drops is introduced cocurrently in the carrier fluid. The dispersed-phase distributor consists of 73 calibrated stainless steel tubes of 1-mm internal diameter mounted inside the convergent section. Figure 2

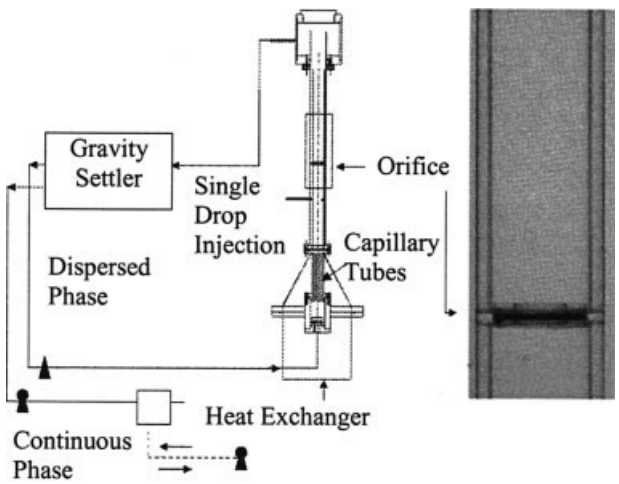

Figure 1. Experimental setup.

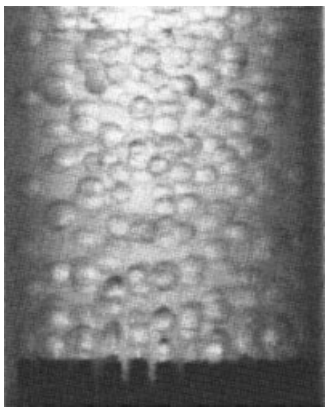

Figure 2. Injection of *n*-heptane drops in upward water flow at the duct bottom.

illustrates the injection of *n*-heptane drops in tap water for a continuous (resp. dispersed) phase flow rate $Q_c = 330$ L/h (resp. $Q_d = 36$ L/h). Changing either the nature of the continuous phase or the flow rate causes the drop diameter to vary from 2 to 3 mm. Because of the monodispersity and the spatial homogeneity of the dispersed phase inside the column, coalescence was never observed upstream to the orifice. The dispersion then flows through a 5-mm thick orifice, which can be easily changed to vary the diameter D_o of the restriction. At the pipe outlet, the liquid–liquid dispersion is continuously separated in a 35-L gravity settler and sent back to the inlet of the column by centrifugal pumps. A heat exchanger controls the temperature of the dispersion in the pipe with an accuracy of 0.1°C.

Two identical transparent test columns made of polymethylmethacrylate (PMMA) were used in this study. The first, dedicated to the measurement of the pressure drop, is equipped with pressure taps on both sides of the orifice connected to a differential pressure transducer. The test section of the second column, dedicated to the measurements by means of high-speed video and PIV, is surrounded by a transparent square box filled with water to reduce optical distortions.

Fluid properties and flow parameters

The physical properties of the fluids are given in Table 1. Concerning breakup, the original results of the present work are all obtained with drops of *n*-heptane (purity 96%) dispersed in an aqueous solution of glycerin (43% in mass). This system, denoted C, allows us to match the refractive index of the aqueous phase to that of *n*-heptane ($n_D = 1.386$ at 29°C) and therefore to investigate highly concentrated dispersions as well as single-phase flows. On the other hand, statistics of drop breakup in single-phase flow of tap water (systems A and B) are issued from Galinat et al.[11] and are recalled here for the purpose of comparison. The addition of glycerin makes the viscosity of the continuous phase of system C about six-fold greater than that of water (systems A and B). Adding red Sudan IV to color the drop decreases the interfacial tension from 47 mN/m for system A down to 24 mN/m for system B. However, it leads to approximately matching the interfacial tension of system B with that of system C.

Table 1. Physical Properties of the Liquid–Liquid Systems*

System	ρ (kg/m^3)	μ (10^{-3} Pa·s)	σ (10^{-3} N/m)
(A) Heptane/water	684/996	0.45/0.82	47
(B) Colored heptane/water	684/996	0.45/0.82	23.6
(C) Colored heptane/water–glycerin	684/1100	0.45/4.7	24.4

*$T = 29$°C.

The operating conditions for breakup experiments of isolated drops in single-phase flow with system C are reported in Table 2. Except for the highest flow rate, the flow regime is laminar upstream of the orifice. Two values of the restriction ratio, $\beta = D_o/D = 1/2$ and 2/3, and six different flow rates are considered. The flow rate may be characterized by either the bulk velocity in the pipe (U) or through the restriction (U_o). For each β, the same range of orifice velocity $0.4 < U_o < 0.9$ m/s was explored, in which the lowest range of maximum pressure drop was observed with $\beta = 2/3$.

The operating conditions of breakup experiments with a colored drop in a concentrated dispersion are listed in Table 3. The concentration of the dispersed phase is characterized by the flow rate ratio upstream of the orifice, defined as follows:

$$\phi_d = \frac{Q_d}{Q_d + Q_c} \tag{2}$$

Note that ϕ_d equals the volume fraction of the dispersed phase ϕ, for a vanishing slip velocity between the two phases. We can estimate the slip velocity by using the drag law identified by Augier et al.[12] for highly concentrated liquid–liquid homogeneous dispersed flows. In the range of parameters considered here, this law predicts that ϕ varies from 0.07 to 0.18 when ϕ_d varies from 0.1 to 0.2. Downstream of the orifice, the occurrence of breakup decreases the drop diameter and tends to reduce the difference between ϕ and ϕ_d. A single aspect ratio, $\beta = 1/2$, and two different concentrations, $\phi_d = 0.1$ and 0.2, have been investigated with orifice velocities U_o ranging between 0.5 and 1.2 m/s.

Instrumentation

The transparent test section and the matching of the fluid indices allows us to use modern optical measurement techniques that give access to the short times and small length scales involved in the hydrodynamics of the drop breakup. The high-

Table 2. Flow Parameters for Water–Glycerin Single-Phase Flow

		$\beta = 1/2$		$\beta = 2/3$	
U (m/s)	Re	U_o (m/s)	ΔP_{max} (Pa)	U_o (m/s)	ΔP_{max} (Pa)
0.118	830	0.472	165	—	—
0.138	970	0.552	251	—	—
0.157	1100	0.628	320	—	—
0.177	1240	0.708	415	—	—
0.196	1380	0.784	525	0.441	95
0.216	1520	—	—	0.486	156
0.236	1660	0.944	765	0.531	187
0.256	1800	—	—	0.576	221
0.294	2060	—	—	0.662	301
0.334	2350	—	—	0.752	396

Table 3. Flow Parameters for Two-Phase Flows with System C*

$\phi_d = 0.1$		$\phi_d = 0.2$	
U_o (m/s)	ΔP_{max} (Pa)	U_o (m/s)	ΔP_{max} (Pa)
0.55	226	—	—
0.64	274	0.62	284
0.76	392	—	—
0.88	492	0.88	501
0.98	637	0.98	617
1.15	874	1.13	811
—	—	1.19	900

*$\beta = 1/2$.

speed PIV and drop imaging techniques used for the measurement of the instantaneous flow field and drop-center coordinates downstream of the orifice are presented.

High-speed PIV. A high-speed particle image velocimetry technique was developed to measure the local instantaneous two-dimensional velocity fields of the continuous phase in single-phase flow as well as in two-phase flow. Because no local measurement of the continuous phase was provided in Galinat et al.,[11] the present investigation of the single-phase flow configuration is not limited to the water–glycerin flow (which is useful to analyze the breakup of isolated drop for system C) and the hydrodynamic field in single-phase flow of water is also presented (for the analysis of drop breakup with systems A and B).

The PIV technique is based on the measurement of the displacement between two successive recorded images of small seeding particles that follow the flow as tracers.[13,14] In the present case, the tracers are fluorescent particles of PMMA, the diameters of which range between 20 and 50 μm. A continuous 7-W argon laser source (Spectra-Physics 2017, Newport Corp., Irvine, CA) is used to generate a thin laser sheet in a median plane of the duct above the orifice. A CMOS high-speed video camera (Photron APX, Digital West Imaging, El Cajon, CA) is used to record images of the flow. The use of a pass-band filter allows the camera to collect only the light emitted by the fluorescent tracers, stopping all parasite reflections from the walls. The choice of the acquisition frequency of the camera depends on the flow velocity and spatial resolution. In the present study, it was set to 0.5 ms. Image size is 512×1024 pixels, corresponding to a 30×60-mm flow section. The velocity is computed using the processing software DaVis 6.2 (LaVision GmbH, Göttingen, Germany). Recorded images are divided into square interrogation windows, within which the gray-level cross-correlation function between two successive images is calculated. Coordinates of the maximum peak of the cross-correlation give the most probable displacement of the fluid. The accuracy of the result is enhanced by a Gaussian interpolation of the cross-correlation peak and by the application of an iterative procedure, involving a decrease of the window size (from 64×64 to 16×16 px^2) and a spatial shift. A detailed description of these techniques is available in Raffel et al.[15] and Fincham and Delerce.[16]

Application of the PIV technique to dispersed flows is made possible by the adjustment of the refractive index of both phases, as was already done by Adrian[17] for solid–liquid flows and by Augier et al.[12,18] for liquid–liquid flows. The PMMA tracers used in the present study are hydrophilic. For that reason, they remain in the aqueous continuous phase without diffusing in the organic dispersed phase. Because there is no tracer inside, drops appear as black regions in the recorded images. The cross-correlation algorithm therefore detects only the displacements of the continuous phase. However, the accuracy in the computed velocity is affected by the presence of the black regions. The initial size of the interrogation windows must be larger than the drop diameter to contain a minimum number of visible tracers. This condition was achieved with windows of 64×64 pixels, which are about twofold larger than the drops. Similarly to single-phase flow, an iterative procedure is used to improve the accuracy. Because of the presence of the black regions, a few erroneous vectors may remain in the velocity field. They are filtered by using a criterion based on the signal-to-noise ratio of the cross-correlation function and replaced by spatially interpolated values. This method is found to be reliable for dispersed-phase concentration up to 0.2.

High-speed Drop Imagery. The image acquisition and processing system used in this study for the measurement of the instantaneous drop coordinates is similar to that used in Galinat et al.[11] Depending on the test case, two different high-speed video cameras were used: an HCC1000 camera with a resolution of 1024×256 pixels and a Photron APX with a resolution of 1024×512 pixels. Both are operated at 500 frames/s with an exposure time of 1/10,000 s, the zone of interest being illuminated with a 1000-W halogen light source. It is worth noting that because only one camera is used for each experimental run, we have access to the projection of the drop motion only in the vertical plane of view. The measurement field is a rectangular window that starts from the orifice and ends 100 mm downstream. Because it was confirmed that no breakup occurred further downstream, this window was large enough to capture all breakup events. The residence time of each drop in the measurement window is about 0.2 s. The acquisition duration was in all cases much larger, about 1 s with the HCC1000 and 24 s with the Photron: successive individual drops trajectories could therefore be stored during a single acquisition run.

Drop characteristics are obtained by digital image processing. Using the Visilog 5 library (ITS–Noesis, Oxnard, CA), we developed an algorithm that involves four steps:

(1) The reference image in the absence of the drop is subtracted to the current image.

(2) The drop contour is obtained by application of a gray-level threshold.

(3) Drops present in the image are labeled.

(4) Geometric properties of each drop are calculated from the contour points.

Finally, the time evolution of the coordinates of the center of each drop, the instant of breakup, and the number and the size of the fragments are obtained. For each set of experimental parameters (U_o, β, and ϕ_d), 60 to 80 drops were tested.

Flow Characterization

This section is devoted to the investigation of the flow of the dispersed mixture downstream of the restriction. The objective is to obtain a detailed description of the fluctuations responsible for the drop deformation and breakup. Yet, it is worth noting that a local description of the velocity field at concentration as large as 0.2 is also of interest for the study of two-phase flow

dynamics, particularly with respect to modeling the turbulence in dispersed flows.

Maximum pressure drop

Percy and Sleicher[19] and Galinat et al.[11] showed that the maximum pressure drop across the orifice, $\Delta P_{\max}$, is the relevant global parameter to characterize the breakup of an isolated drop downstream of a restriction. In single-phase flow,[20] $\Delta P_{\max}$ is well described by the empirical correlation

$$\Delta P_{\max} = \frac{1}{C_{\mathrm{Do}}^2}\,\frac{1}{2}\,\rho U^2\left(\frac{1}{\beta^4}-1\right) \tag{3}$$

The orifice coefficient C_{Do} depends on the restriction ratio β, the Reynolds number, and the exact geometry of the orifice. Axial profiles of static pressure downstream of the orifice in dispersed two-phase flows were measured for various concentrations and Reynolds numbers. These profiles are similar to those obtained in single-phase flow, exhibiting a maximum located at one pipe diameter downstream of the orifice. For a fixed value of the restriction ratio ($\beta = 1/2$), Figure 3 depicts the evolution of $\Delta P_{\max}$ against the global kinetic energy of the mixture, $1/2\rho U^2$, for six different concentrations ranging from zero to 0.2. In all cases, $\Delta P_{\max}$ is an increasing linear function of the global kinetic energy, but its slope depends on the case under consideration. The presence of a small concentration of drops ($\phi_d = 0.025$) is sufficient to cause a significant decrease of the slope relative to the single-phase flow of water–glycerin ($\phi_d = 0$), but further increasing the concentration, from 0.025 to 0.2, no longer influences the slope. The weak influence of the concentration on the maximal pressure drop downstream of a restriction was already reported by Pal[21] with stable liquid–liquid emulsions in all ranges of concentrations and Reynolds numbers.

In Figure 3, results obtained with a single-phase flow of water are also reported (white squares). The slope of $\Delta P_{\max}$ for the water flow is lower than that of water–glycerin. This is a consequence of the decrease of the Reynolds number by a factor close to 5.5, as the flow viscosity is increased. Note that in this case, the $\Delta P_{\max}$ curve is very close to that of the dispersed two-phase flow with system C for $\phi_d \geq 0.025$, but no valuable conclusion can be drawn from that result.

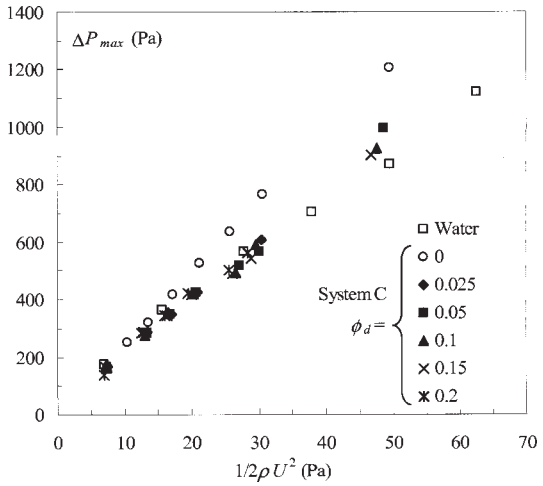

Figure 3. Maximum pressure drop ($\beta = 1/2$) as a function of the bulk flow kinetic energy.

The evolution of the global parameter $\Delta P_{\max}$ suggests the following remarks. First, in this range of Reynolds number, the flow configurations under investigation are still dependent on the Reynolds number. Second, the effect of the concentration on $\Delta P_{\max}$ is clearly different from that of the viscosity. Thus, the effect of the dispersed phase on the flow structure cannot be accounted for by a consistent increase of the mixture viscosity.

Local flow structure downstream of the orifice

This section presents PIV measurements of the flow downstream of the restriction for an orifice velocity $U_o = 0.60$ m/s and a restriction ratio $\beta = 1/2$. Four cases are investigated: (1) a single-phase flow of water (Re = 2000), (2) a single-phase flow of water–glycerin (Re = 11,000), and two dispersed flows with system C at (3) $\phi_d = 0.1$ and (4) $\phi_d = 0.2$. Note that in the case of two-phase flows, only the velocity of the continuous phase is measured. In all cases, velocity components are measured in a vertical plane containing the pipe axis. Given that the flow is turbulent, time-averaged quantities have been reported: the mean axial velocity (U_x) and the standard deviation (u_x) of the axial velocity.

Mean Axial Velocity. Figure 4 reports the radial profiles of U_x at different axial distances from the orifice ($x = 10$, 20, 30, 40, and 50 mm) for the four cases investigated. The flow structure is similar for all cases: the acceleration through the orifice produces an axisymmetric jet that spreads in the radial direction and reattaches to the pipe wall beyond the limit of the measuring window ($x = 60$ mm). A large recirculation zone therefore surrounds the jet downstream of the orifice. All profiles exhibit a good axial symmetry, suggesting that the jet is well centered in the pipe. Close to the orifice, U_x profiles are flat, indicating the existence of a potential core. The increase of the flow rate observed along the jet axis right after the orifice compensates the reverse flow in the recirculation region close to the wall (negative velocity in Figure 4). The maximum of the centerline velocity $U_{x\max}$, located at $x = 10$ mm ($\approx 0.3D$), equals $1.25U_o$ with the single-phase flow of water (Figure 4a) and $1.10U_o$ with the water–glycerin flow. In the case of an air flow at Re $= 10^5$ with $\beta = 1/2$, Morrison et al.[22] obtained similar results: a maximal velocity located at $x/D \approx 0.37$ and a maximal pressure drop located at $x/D \approx 1$. The profiles spread as x increases and beyond $x = 10$ mm, $U_{x\max}$ continuously decreases. Because of the lateral confinement, the radial location of the maximum of the velocity gradient remains close to 7.5 mm, which corresponds to the edge of the orifice ($D_o/2$).

However, the flow deceleration is not identical in each studied case. In single-phase flow, it is larger for the water flow at $\mathrm{Re}_o = 11{,}000$ (Figure 4a) than for the water–glycerin flow at $\mathrm{Re}_o = 2000$ (Figure 4b), as a result of the increase of turbulent diffusion with the Reynolds number. For the same reason, the water flow also reattaches sooner to the pipe wall.

Axial velocity profiles obtained in two-phase flows (Figures 4c and 4d) exhibit a stronger diffusion of U_x, which is probably caused by an enhancement of the turbulence production by the drops. It must be pointed out that the effect of increasing the drop concentration from 0 to $\phi_d = 0.10$ (Figure 4c vs.

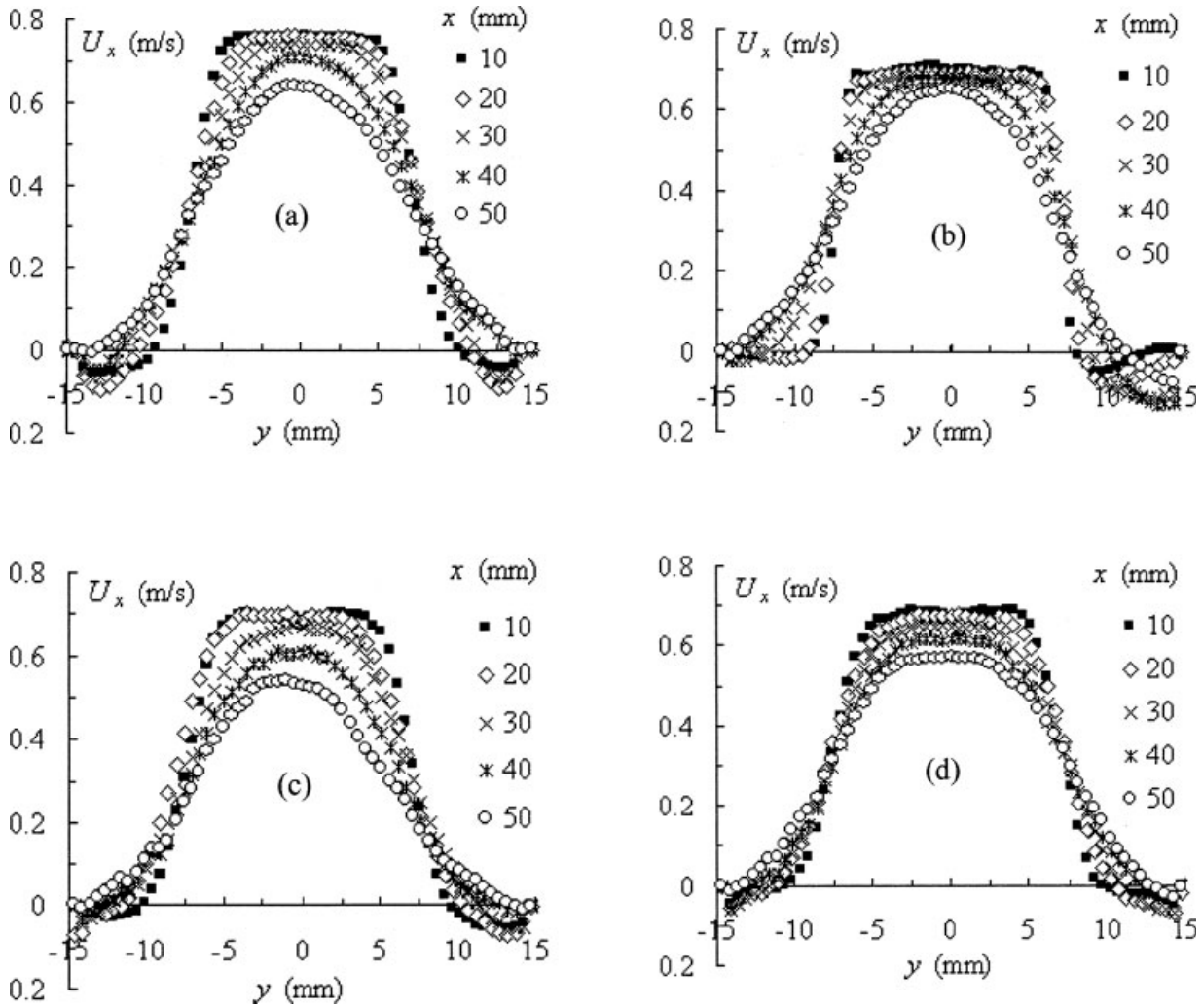

Figure 4. Mean axial velocity profiles at different cross sections downstream of the orifice.

$U_o = 0.60$ m/s, $\beta = 1/2$. (a) Water; (b) water–glycerin; (c) system C with $\phi_d = 0.1$; (d) system C with $\phi_d = 0.2$.

Figure 4b) on the jet diffusion is more important than that of increasing the Reynolds number by a factor 5.5 in single-phase flow (Figure 4b vs. Figure 4a). A significant increase of the radial diffusion of the axial mean velocity profile was previously reported in the case of turbulent mixing layers, even at low concentrations: the bubbly case was experimentally investigated by Roig et al.,[23] whereas the liquid–liquid case was studied by Augier.[24] In the present case, the role of the dispersed phase is not simple because the increase of diffusion of the mean velocity is observed to be weaker at $\phi_d = 0.2$ (Figure 4d) than at $\phi_d = 0.1$ (Figure 4c).

Axial Velocity Fluctuations. Profiles of the axial velocity fluctuation u_x are reported in Figure 5. In all cases, they exhibit two symmetrical peaks at the radial position $D_o/2 = 7.5$ mm (above the orifice edge). As x increases, their base spreads and their intensity slightly increases.

In single-phase flow, the turbulence peak spreads faster at Re = 11,000 (Figure 5a) than at Re = 2000 (Figure 5b). However, the maximum levels of the fluctuations are close ($u_{x\max} = 0.18$ m/s in water, 0.16 m/s in water–glycerin) and the turbulence intensity of both cases is in agreement with the value obtained at Re = 10^5 by Morrison et al.,[22] $(u_{x\max}/U_{x\max})^2 = 0.057$. On the other hand, examination of the radial fluctuations (not reported here) shows that the isotropy ratio, u_r/u_x, remains close to 1.5 for $x \geq 20$ mm.

In the case of two-phase flow, the same level of maximum fluctuation is observed with both $\phi_d = 0.10$ (Figure 5c) and $\phi_d = 0.20$ (Figure 5d) and $u_{x\max} \approx 0.2$, which corresponds to a turbulent intensity, $(u_{x\max}/U_{x\max})^2 = 0.09$, much higher than that in the single-phase flow of water–glycerin (Figure 5b). Moreover, in two-phase flow, this maximum is located near the orifice ($x \leq 10$ mm), whereas in single-phase flow, it is reached at the end of the measurement window ($x \geq 50$ mm). It also seems important to mention that, in the vicinity of the orifice, the width of the turbulence peak is larger in two-phase than in single phase flow cases. We can thus expect that the probability that a drop encountering strong turbulent fluctuations close to the orifice is larger in two-phase flow than in single-phase flow. The increase of the axial velocity fluctuations is concomitant with a slight decrease of the radial fluctuations (not reported here), resulting in an increase of the turbulence anisotropy. Similarly to what was observed with the mean velocity, the effect of the drop presence on the velocity fluctuations changes with the drop concentration.

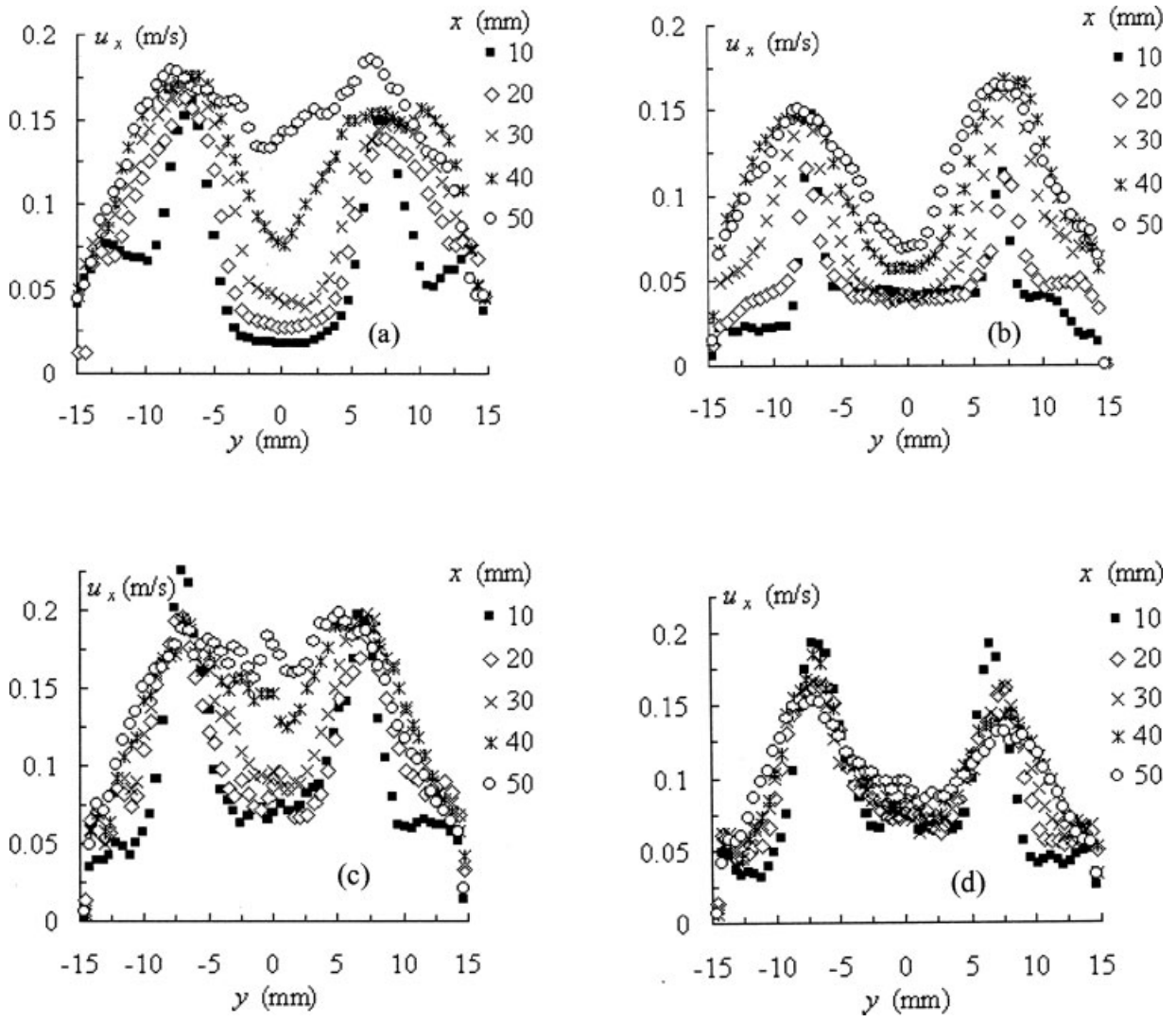

Figure 5. Axial velocity fluctuations profiles at different cross sections downstream of the orifice.

$U_o = 0.60$ m/s, $\beta = 1/2$. (a) Water; (b) water–glycerin; (c) system C with $\phi_d = 0.1$; (d) system C with $\phi_d = 0.2$.

For $\phi_d = 0.1$ (Figure 5c), velocity fluctuations diffuse much faster toward the pipe center compared to both single-phase (Figure 5b) and two-phase flow cases at $\phi_d = 0.2$.

An increase of the intensity of the fluctuations with the dispersed-phase concentration was previously observed in various dispersed flows, such as homogeneous bubbly flows[23,25,26] or liquid–liquid flows.[27] At moderate concentration, the contribution of the dispersed phase to the global turbulent energy of the continuous phase generally scales as ϕU_R^2, where U_R is the slip velocity between the two phases. Moreover, the increase of diffusion of the velocity gradient in a homogeneous bubbly shear flow can be modeled through a modified eddy viscosity. A first model for the contribution v_{TP}^t of the dispersed phase to the eddy viscosity was proposed by Sato et al.[28]:

$$v_{TP}^t \propto \phi d U_R \tag{4}$$

where d is the diameter of the bubbles or drops. More recently, Chahed et al.[29] and Bellakhel et al.[30] proposed a more sophisticated expression that models the enhanced turbulence production and eddy stretching by the bubbles:

$$v^t = v_0^t \frac{1 + C(k_s/k_0)}{1 + \phi(\tau^t/\tau_b)} = v_0^t \frac{1 + C'\phi U_R^2/k_0}{1 + \phi U_R \tau^t/d} \tag{5}$$

where v_0^t, k_0, and τ^t are, respectively, the eddy viscosity, the fluctuating kinetic energy, and the turbulence time macroscale of the carrier flow in the absence of bubbles, where C' is a dimensionless constant of order one. Applied to a bubbly shear layer with a uniform bubble concentration, this model manages to predict the increase of the mixing layer width. Qualitatively, Eq. 5 also seems able to reproduce the general trend of the turbulent flow downstream of the orifice. Indeed, it may predict the increase of the jet diffusion when the drop concentration increases from 0 to 0.1. It may also reproduce the attenuation of the diffusion observed when the concentration increases from 0.1 to 0.2. However, using the drag force correlation, proposed by Augier et al.[12] to estimate the slip ve-

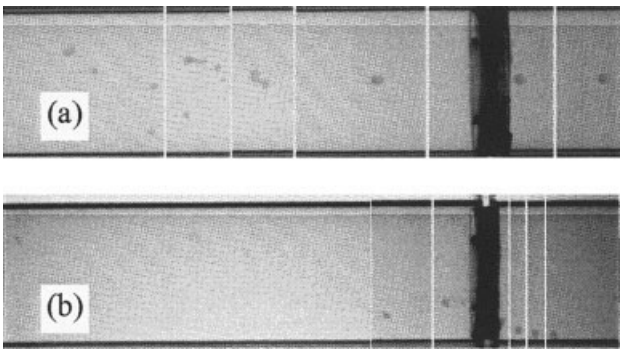

Figure 6. Video sequence of drop breakup downstream of the orifice (the time interval is 20 ms).

System C, $U_o = 0.92$ m/s, $\beta = 1/2$. (a) $\phi_d = 0$; (b) $\phi_d = 0.2$.

locity, the estimation of ϕU_R^2 represents only 2.5% of the fluctuating kinetic energy of the continuous phase. A model like Eq. 5 thus cannot account quantitatively for the present results. The diffusion of the velocity gradient downstream of the orifice is not controlled only by the eddy viscosity—the inertia of the drop and the gradient of the concentration probably also play major roles.[31]

Local velocity measurements have shown the dependency of the turbulent flow downstream of the orifice with the drop concentration. On the one hand, the presence of drops is responsible for a faster decrease of the mean axial velocity and for an increase of the turbulent intensity. On the other hand, the location and extension of the regions of most intense turbulence are very different in the four cases under consideration. Significant differences concerning drop breakup spatial distribution may thus be anticipated.

Statistics of Drop Breakup over the Whole Test Section

The behavior of drops downstream of the orifice was recorded by means of high-speed imaging. Figure 6 shows two typical sequences of the breakup of a colored drop (system C) in single-phase flow (Figure 6a) and in dispersed two-phase flow at $\phi_d = 0.2$ (Figure 6b). In both cases, the drop is elongated, takes a dumbbell shape, and eventually breaks into two or more fragments. However, occurrence of breakup is mainly observed right after the orifice in the two-phase flow case, whereas in the single-phase flow case, it is preferentially localized in the upper part of the test section. In all cases, however, breakup was never observed outside the measurement window.

Several test cases were investigated with system C, the flow parameters of which are listed in Table 2 for $\phi_d = 0$ and in Table 3 for $\phi_d = 0.1$ and 0.2. For each configuration, about 70 colored drops of *n*-heptane with diameters ranging from 1.4 to 2 mm were injected upstream of the orifice and their motions recorded with a high-speed camera. In case of breakup, the location of breakup and the properties of the resulting fragments are determined using a digital image processing technique. Breakup statistics are then estimated for each flow configuration.

With respect to engineering applications, the knowledge of breakup probability at the crossing of a duct singularity is an important issue. Galinat et al.[11] determined the breakup statistics at the scale of a finite volume downstream of the restriction. In this section, the same analysis is repeated: the evolution of the (1) global probability of breakup in the test section, (2) the mean number of fragments, and (3) the mean and Sauter diameter of the daughter drops are reported as a function of the global Weber number based on the maximum pressure drop across the orifice (Eq. 1). The spatial distribution of breakup events and its relation with the local turbulence field will be considered in next section.

Breakup probability

Figure 7 reports the evolution of the breakup probability as a function of the global Weber number in a single-phase flow of water–glycerin (system C). The results obtained for two different orifice ratios, $\beta = 1/2$ and $\beta = 2/3$, are similar. Experimental data are compared with the fitting curve of the results obtained with systems A and B (dotted line) by Galinat et al.[11] System C shows a similar evolution compared to that of systems A and B, although we may note that the breakup probability for system C is, at the largest values of the Weber number, slightly below that for systems A and B. In the investigated range of parameters, increasing the viscosity by a factor > 5 does not significantly influence the breakup probability, which therefore still depends only on We. The validity of the breakup correlation proposed by Galinat et al.[11] can thus be extended to a broader range of flow Reynolds numbers. A possible explanation for this result could be that, even if the local structure of the turbulent flow is modified by the addition of glycerin, the maximum level of turbulent fluctuations is about the same.

Figure 8 shows the evolution with the Weber number of the breakup probability of a colored drop in dispersed two-phase flow at ϕ_d values of 0.1 and 0.2. These results were obtained by varying the bulk velocity for a fixed restriction ratio, $\beta = 1/2$. In this graph, single-phase flow results were fitted by a power law (dotted line). No differences are visible between the two-phase flow case at $\phi_d = 0.1$ and the single-phase case, whereas the breakup probability is significantly lower

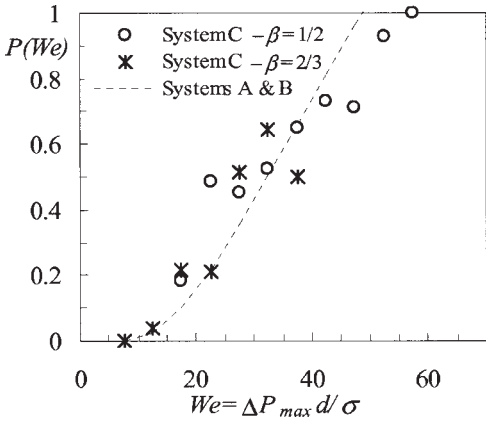

Figure 7. Breakup probability vs. Weber number.

The dashed line is the fitting curve obtained with systems A and B.

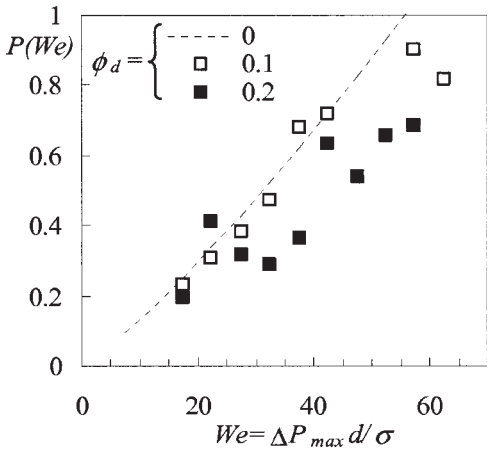

Figure 8. Breakup probability vs. Weber number in concentrated dispersions.

System C, $\beta = 1/2$. The dashed line is the fitting curve obtained with $\phi_d = 0$.

for $\phi_d = 0.2$, especially at large We. This result clearly states that a global Weber number based on the maximum pressure drop, ΔP_{max}, cannot provide a unique scaling law for breakup, including the influence of concentration. In addition, the description of turbulent flow obtained in section 3 suggests that no Weber number based on any global flow property would manage to collapse the results obtained at various concentrations. Indeed, for a given ΔP_{max}, the values of the bulk kinetic energy are the same for $\phi_d = 0.1$ and $\phi_d = 0.2$. Moreover, the maximal velocity fluctuations u_{xmax} are close and the turbulent intensity $(u_{xmax}/U_{xmax})^2$ is about the same in both cases. A similar conclusion would be drawn with the global dissipation rate $(U\Delta P_{max})$ across the orifice.

It can be concluded that the breakup probability is well described by a unique function of the sole global Weber number for orifice Reynolds numbers in the range from 2000 to 11,000 and concentrations up to 0.1. For larger drop concentrations, a global Weber number is not sufficient.

Mean number of fragments and daughter-drop diameter

Characteristics of the daughter drops resulting from breakup are now considered. Note that whenever a drop undergoes successive breakup, the statistics are estimated from the final daughter-drop population.

Results obtained with colored drops in a single-phase flow of water–glycerin (system C, $\phi_d = 0$) for two orifice ratios ($\beta = 1/2$ and $\beta = 2/3$) are first examined. Figure 9a shows the mean number of fragments N_f as a function of the global Weber number. N_f remains close to 2 for We < 40 and then increases as We increases. The standard deviation of the number of fragments (n_f, half of the vertical bars in Figure 9a) and the Sauter diameter (d_{d32}) of the daughter drops (Figure 9b) evolve in the same way: a very weak slope at low We followed by a monotonic increase (resp. decrease) of n_f (resp. d_{d32}/d). Binary breakup is thus dominant at low Weber numbers, whereas for We > 40 an increasing number of fragments are produced as We increases. Dotted lines in Figure 9a (resp. 9b) are the fitting curves of N_f (resp. d_{d32}/d) measured by Galinat et al.[11] with both colored and noncolored drops in a single-phase flow of water (systems A and B). These previous results obtained at a higher Reynolds number follow the same trend: they display only a slightly faster increase (resp. decrease) of N_f (resp. d_{d32}/d) with We.

Results obtained in dispersed flows with system C (with $\beta = 1/2$) are plotted in Figures 10a and 10b. Plain symbols correspond to the concentrated cases $\phi_d = 0.1$ and $\phi_d = 0.2$, whereas the dotted line fits the results obtained at $\phi_d = 0$. The mean number of fragments (Figure 10a) and the daughter-drop Sauter diameter (Figure 10b) follow the same evolution in two-phase flow as in single-phase flow.

Local Analysis of the Drop Breakup

The analysis of drop breakup statistics at the scale of the whole pipe singularity shows that the breakup probability and the number of fragments are increasing functions of a global Weber number based on the maximum pressure drop across

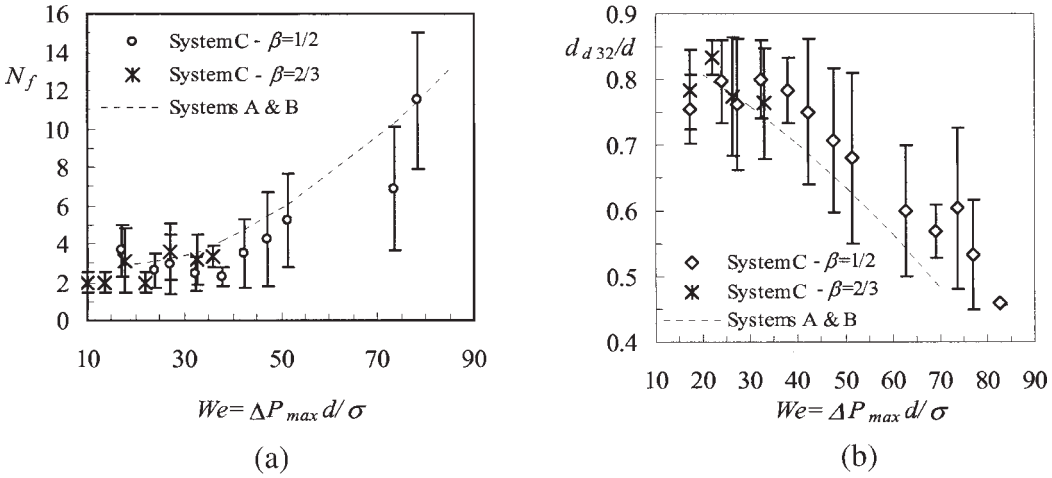

Figure 9. (a) Mean number of fragments (vertical bars represent ± standard deviation (SD); the dashed line is the fitting curve obtained with systems A and B); (b) reduced daughter-drop Sauter diameter vs. Weber number (vertical bars represent ± SD; the dashed line is the fitting curve obtained with systems A and B).

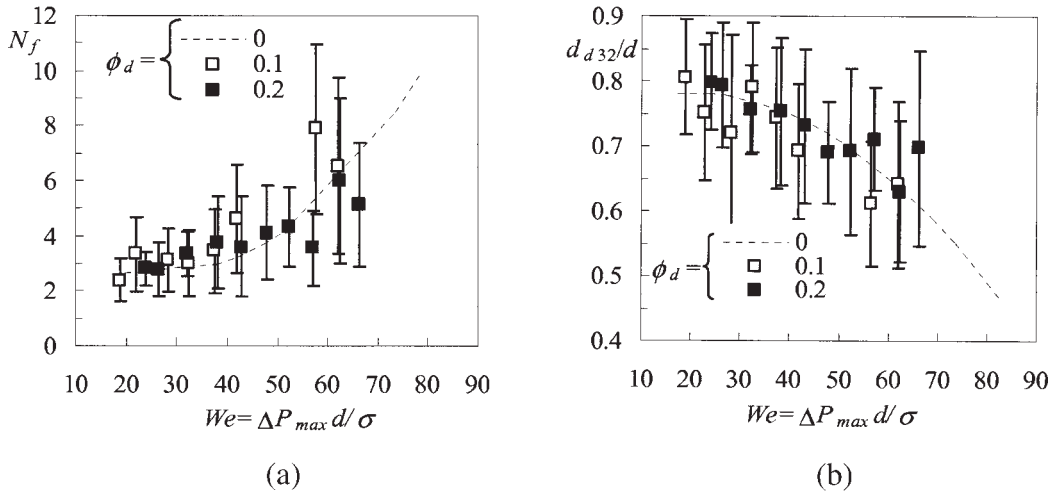

Figure 10. (a) Mean number of fragments in concentrated dispersions (system C, β = 1/2; vertical bars represent ± SD; the dashed line is the fitting curve obtained with ϕ_d = 0); (b) reduced daughter-drop Sauter diameter vs. Weber number in concentrated dispersions (system C, β = 1/2; vertical bars represent ± SD; the dashed line is the fitting curve obtained with ϕ_d = 0).

the orifice. As a consequence, the Sauter diameter of the daughter drops decreases as the Weber number increases. These parameters adopt the same behavior in single-phase flows as that in two-phase flows, suggesting that the breakup is not influenced by the concentration in the range $0 \leq \phi_d \leq 0.1$. However, the growth rate of breakup probability for We $\geq$ 30 is smaller at $\phi_d = 0.2$ than that at $\phi_d \leq 0.1$. The PIV measurements showed that an increase in the drop concentration from $\phi_d = 0$ to $\phi_d = 0.1$ causes an increase of 25% in the maximum fluctuation $u_{x\max}$, whereas an increase from $\phi_d = 0.1$ to $\phi_d = 0.2$ does not cause any significant increase of $u_{x\max}$. Therefore, the observed evolution of the breakup probability cannot be simply related to a variation of the turbulence intensity, nor can it be explained by the increase of the effective viscosity of the two-phase mixture with the concentration because the addition of glycerin in water increases the viscosity more than fivefold without significantly changing the probability of breakup. Thus, the evolution of the relationship between the breakup probability and the global Weber number is likely to result from local changes in the spatial structure of the turbulence field downstream of the orifice.

Figure 11 reports the spatial distribution of the axial fluctuation u_x downstream of the orifice ($0 \leq x \leq 60$ mm) for U_o = 0.6 m/s and β = 1/2. The same four cases as in Figures 4 and 5 are presented: a single-phase flow of water at Re = 11,000 (Figure 11a), a single-phase flow of water–glycerin at Re = 2000 (Figure 11b), and two dispersed flows of *n*-heptane drops in water–glycerin at $\phi_d = 0.1$ (Figure 11c) and $\phi_d = 0.2$ (Figure 11d). In each subfigure, drop breakup events are localized by circles. Note that contrary to the turbulent field, which is actually measured in a meridian plane, these symbols correspond to the projection in the plane of view of the three-dimensional position of the drops: the axial coordinate is therefore exact, although the radial one is equal to or smaller than the actual one. In all cases, the turbulence is generated in the mixing layer that develops at the periphery of the jet and than diffuses radially as the distance from the orifice increases. The regions of less-intense turbulence therefore correspond to the jet core and the recirculating zone around the jet. However, this common global structure of the turbulent fields does not exclude the presence of strong differences between the four cases.

In single-phase flow, the annular layer of intense turbulence is larger and diffuse faster at Re = 11,000 (Figure 11a) than at Re = 2000 (Figure 11b). In both cases, breakup events are never located in the central region where the turbulence is weak. At Re = 11,000, breakup is observed in two distinct zones: (1) in the region of intense turbulence production located just downstream of the orifice ($x \leq 20$ mm) and (2) further downstream ($x \geq D = 30$ mm). At Re = 2000, breakup no longer occurs close to the orifice but is still observed one pipe diameter downstream ($x \geq D = 30$ mm).

Compared to the single-phase case at the same Reynolds number (Figure 11b), two-phase flow distributions of u_x at $\phi_d = 0.1$ (Figure 11c) and $\phi_d = 0.2$ (Figure 11d) exhibit, just downstream of the orifice, a larger intensity distributed over a wider annular region. The turbulence levels of cases $\phi_d = 0.1$ and $\phi_d = 0.2$ are quite similar near the orifice but significant differences appear when x increases. At $\phi_d = 0.1$, the axial fluctuation in the central region of the pipe increases toward the maximum value, which remains constant. At $\phi_d = 0.2$, the axial fluctuation near the axis increases only very slightly, whereas the maximum value decreases. This evolution of velocity fluctuations with the concentration has severe consequences regarding breakup locations, which accumulate mainly near the orifice in two-phase flow cases. At $\phi_d = 0.2$ (Figure 11d), no breakup is observed even for x values larger than one pipe diameter, at the exact opposite of what is observed at $\phi_d = 0$ (Figure 11b).

Because the breakup locations are strongly related to the heterogeneous structure of the turbulence, it is interesting to consider the evolution of breakup probability with the distance from the orifice. Figure 12 depicts the distribution function $F(x)$ of the breakup occurrences, that is, the probability that a

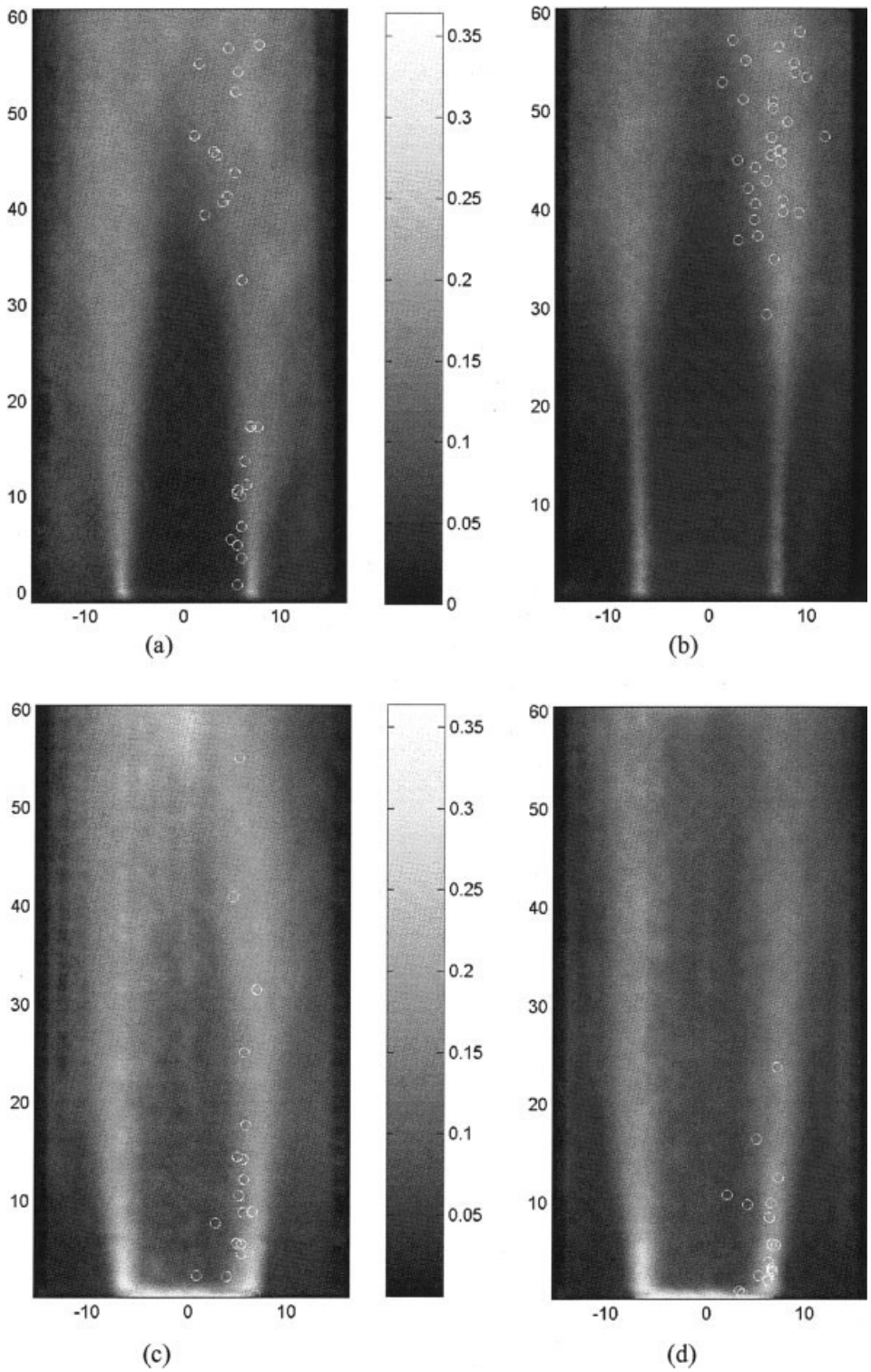

Figure 11. Axial velocity fluctuation distributions downstream of the orifice (m/s).

$U_o = 0.60$ m/s, $\beta = 1/2$. (a) Water; (b) water–glycerin; (c) system C with $\phi_d = 0.1$; (d) system C with $\phi_d = 0.2$. Open symbols represent the breakup locations.

drop breaks at a distance smaller than x. The cumulated probability $F(x)$, presented for the same four cases, reinforces the conclusions drawn from the analysis of Figure 11. In all cases $F(x)$ reached unity before $x = 80$ mm, indicating that all breakup events occur in the region under investigation. For the single-phase flow at Re = 11,000, the horizontal tangent observed close to $x = 30$ mm is the signature of the existence of a region where no breakup occurs, surrounded upstream and

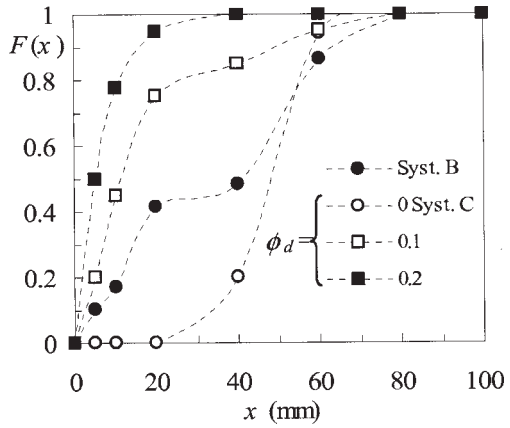

Figure 12. Distribution function of breakup axial locations.

downstream by two regions where it does. For the single-phase flow of water–glycerin, the S-shape shows that breakup is no longer possible close to the orifice and occurs exclusively for $x \geq 30$ mm at Re = 2000. In two-phase flow cases, the sign of the curvature of $F(x)$ always remains negative, indicating the existence of a unique region of breakup that starts just downstream of the orifice, where the breakup probability is maximum and ends at $x = 80$ mm (resp. 40 mm) for $\phi_d = 0.1$ (resp. 0.2).

Breakup probability is thus strongly related to the local structure of the turbulence field downstream of the orifice. The condition for breakup to occur requires that a drop crosses a region of intense turbulence, where the order of magnitude of the instantaneous velocity fluctuations is given by $u_{x\max} \approx 0.2$ m/s. This confirms that in such flows, in which the Reynolds number based on d and $u_{x\max}$ is always >100, the drop deformation is driven by the pressure fluctuations at the scale of the drop, according to the inertial turbulent breakup mechanism first described by Kolmogorov[32] and Hinze.[33] Moreover, the maximum turbulence intensity is well correlated to the maximum pressure drop. Within the range of Reynolds number and drop concentration considered, a global Weber number based on $\Delta P_{\max}$ could be a priori relevant for characterizing the main features of the drop breakup statistics at the scale of the pipe singularity. However, the complex modifications in the spatial distribution of the turbulence that occur when the flow configuration is changed are not determined by the maximum pressure drop. Thus, breakup probability over the whole test section, which also depends on the volume of the region in which the most intense turbulent fluctuations are observed, cannot be fully determined by the global Weber number. In particular, the smaller breakup probability observed at $\phi_d = 0.2$ compared to ϕ_d values of 0 and 0.1 (Figure 8) is explained by a severe reduction of the volume of the region of intense turbulence.

Conclusions

The present study provides original results concerning the breakup of drops in a dispersed two-phase turbulent flow downstream of an orifice. Through use of the optical index matching technique and high-speed video imaging, the behavior of colored drops of *n*-heptane were investigated in both a single-phase flow of water–glycerin ($\phi_d = 0$) and dispersed flows of *n*-heptane drops in water–glycerin at concentrations $\phi_d = 0.1$ and $\phi_d = 0.2$. In a first step, breakup statistics over the whole test section were represented as a function of the global Weber number based on the maximum pressure drop across the orifice. The evolutions of the mean number of fragments and the daughter-drop Sauter diameter were found to be similar at ϕ_d values of 0, 0.1, and 0.2, extending the validity of the scaling laws proposed by Galinat et al.[11] for heptane drops in a single-phase flow of water at a larger Reynolds number. On the other hand, the probability of drop breakup downstream of the orifice is well described by an increasing function of the unique global Weber number for single-phase flows at various Reynolds numbers and two-phase flows at $\phi_d = 0.1$. However, at $\phi_d = 0.2$, breakup probability is found to be smaller for We ≥ 30. This behavior is understood from the local structure of the turbulence, which was characterized by means of high-speed PIV.

In all cases, breakup occurs in the regions of intense turbulence, which can be characterized by their location, volume, and maximum fluctuation. Because the maximum fluctuation level scales with the maximum pressure drop and is always large enough for the breakup to be driven by an inertial mechanism, breakup statistics primarily depend on the global Weber based on $\Delta P_{\max}$. However, this parameter is not relevant for characterization of the location and volume of the regions of intense turbulence, which change considerably when either the Reynolds number or the drop concentration vary. In particular, the annular layer of high turbulence around the jet just after the orifice is broader and more intense than that in a single-phase flow. As a consequence, it is not possible to describe the two-phase flow as a single-phase flow of a mixture with average physical properties. This modification of the turbulence induced by the drops is responsible for a diminution of the volume of the region within which turbulence is large enough to cause breakup, explaining the smaller breakup probability observed at $\phi_d = 0.2$. Interestingly, even when the breakup probability over the whole test section is the same in two distinct flow configurations, the evolution of the local breakup probability with the distance from the orifice can be very different.

The present study shows that the global statistics of breakup at the scale of the entire pipe singularity can be correlated to a global Weber number, at least for drop concentrations up to 0.1. This result is nevertheless specific to the present configuration and must not be generalized to any heterogeneous turbulent flow. Breakup probability does not depend only on a global measurement of the turbulence intensity over the whole test section; it also depends on the probability that drops pass through the regions of intense turbulence. With respect to modeling issues of breakup in heterogeneous two-phase turbulence, these results underline the need for accounting for the local turbulent stress experienced by the drop along its trajectory. It probably also requires a correct description of the dynamic response of the drop to the corresponding unsteady turbulent forcing.[34] Future work will be directed toward investigating that feasibility.

Acknowledgments

This work was jointly sponsored by the Institut Français du Pétrole and by the research group FERMaT.

Notation

C_{Do} = orifice coefficient
d = drop diameter, m
d_{32} = Sauter mean diameter, m
d_{d32} = daughter-drop Sauter diameter, m
D = pipe diameter, m
D_o = orifice diameter, m
n_D = refractive index
N_f = mean number of fragments
n_f = standard deviation of the number of fragments
P = breakup probability
Q = flow rate, l/h
Re = pipe Reynolds number ($= DU\rho_c/\mu_c$)
Re_o = orifice Reynolds number ($= D_oU_o\rho_c/\mu_c$)
U = bulk velocity in the pipe, m/s
U_o = bulk velocity through the restriction ($= U/\beta^2$), m/s
U_x = mean axial velocity, m/s
u_x = standard deviation of the axial velocity, m/s
We = global Weber number ($= \Delta P_{max}d/\sigma$)
x = axial distance to the orifice, m

Greek letters

β = restriction ratio between the orifice and the pipe diameter ($= D_o/D$)
ΔP_{max} = maximum pressure drop through the orifice, Pa
ϕ = dispersed phase volume fraction
ϕ_d = dispersed phase flow fraction
μ = dynamic viscosity, Pa·s
ρ = density, kg m^{-3}
σ = interfacial tension, N m^{-1}

Subscripts

c = continuous phase
d = dispersed phase
max = local maximum
r = radial direction
x = axial direction

Literature Cited

1. Risso F. The mechanisms of deformation and breakup of drops and bubbles. *Multiphase Sci Technol*. 2000;12:1–50.
2. Calderbank PH. Physical rate processes in industrial fermentation. I. The interfacial area in gas–liquid contacting with mechanical agitation. *Trans IChemE*. 1958;36:443–463.
3. Sprow FB. Distribution of drop sizes produced in turbulent liquid–liquid dispersion. *Chem Eng Sci*. 1967;22:435–442.
4. Brown DE, Pitt K. Drop breakup size distribution of stirred noncoalescing liquid–liquid system. *Chem Eng Sci*. 1972;27:577–583.
5. Calabrese RV, Wang CY, Bryner NP. Drop breakup in turbulent stirred-tank contactors. Part III: Correlations for mean size and drop size distribution. *AIChE J*. 1986;32:677–681.
6. Doulah S. Effect of hold-up on drop sizes in liquid–liquid dispersions. *Ind Eng Chem Fundam*. 1975;14:137–138.
7. Lagisetty JS, Das PK, Kumar R, Ghandi KS. Breakage of viscous and non-Newtonian drops in stirred dispersions. *Chem Eng Sci*. 1986;41: 65–72.
8. Chatzi EG, Kiparissides C. Steady-state drop-size distributions in high holdup fraction dispersion systems. *AIChE J*. 1995;41:1640–1652.
9. Kumar S, Kumar R, Gandhi KS. Alternative mechanisms of drop breakage in stirred vessels. *Chem Eng Sci*. 1991;46:2483–2489.
10. Desnoyer C, Masbernat O, Gourdon C. Experimental study of drop size distributions at high phase ratio in liquid–liquid dispersions. *Chem Eng Sci*. 2003;58:1353–1363.
11. Galinat S, Masbernat O, Guiraud P, Dalmazzone C, Noik C. Drop break-up in turbulent pipe flow downstream of a restriction. *Chem Eng Sci*. 2005;60:6511–6528.
12. Augier F, Masbernat O, Guiraud P. Slip velocity and drag law in a liquid–liquid homogeneous dispersed flow. *AIChE J*. 2003;49:2300–2316.
13. Lourenco LM. Velocity measurement by optical and digital processing of time exposed particle pairs. *Bull Am Phys Soc*. 1984;29:1531.
14. Adrian RJ, Yao C. Scattering particle characteristics and their effect on pulsed laser measurements of fluid flow speckle velocimetry versus particle image velocimetry. *Appl Optics*. 1984;23:1690–1691.
15. Raffel M, Willert C, Kompenhans J. *Particle Image Velocimetry*. Berlin: Springer-Verlag; 1998.
16. Fincham A, Delerce G. Advanced optimization of correlation imaging velocimetry algorithms. *Exp Fluids*. 2000;29:13–22.
17. Adrian RJ. Particle-imaging techniques for experimental fluid mechanics. *Annu Rev Fluid Mech*. 1991;23:261–304.
18. Augier F, Masbernat O, Guiraud P.Simultaneous volume fraction and velocity measurements in liquid–liquid flows. Proceedings of FEDSM'00, ASME Fluids Engineering Division Summer Meeting, Boston, MA, June 11–15; 2000.
19. Percy JS, Sleicher CA. Drop break-up in the flow of immiscible liquids through an orifice in a pipe. *AIChE J*. 1983;29:161–164.
20. Perry RH. *Chemical Perry's Engineers' Handbook*. 6th Edition. New York: McGraw-Hill; 1984.
21. Pal R. Flow of oil in water emulsions through orifice and Venturi meters. *Ind Eng Chem Res*. 1993;32:1212–1217.
22. Morrison GL, DeOtte RE, Nail GH. Mean velocity and turbulence fields inside a $\beta = 0.50$ orifice flowmeter. *AIChE J*. 1993;39:744–756.
23. Roig V, Suzanne C, Masbernat L. Experimental investigation of a turbulent bubbly mixing layer. *Int J Multiphase Flow*. 1998;24:5–54.
24. Augier F. *Structure locale du champ hydrodynamique dans les écoulements dispersés liquide–liquide concentrés*. PhD Thesis. Toulouse, France: Institut National Polytechnique de Toulouse; 2001.
25. Lance M, Bataille J. Turbulence in the liquid phase of a uniform bubbly air–water flow. *J Fluid Mech*. 1991;222:95–118.
26. Risso F, Ellingsen K. Velocity fluctuations in a homogeneous dilute dispersion of high-Reynolds-number rising bubbles. *J Fluid Mech*. 2002;453:395–410.
27. Augier F, Masbernat O, Guiraud P. Fluctuating motion in a homogeneous liquid–liquid dispersed flow at high phase fraction. Proceedings of the 5th International Conference on Multiphase Flow, ICMF'04, May 30–June 4, Yokohama, Japan; 2004:274.
28. Sato Y, Sadatomi M, Sekoguchi K. Momentum and heat transfer in two-phase bubble flow—I. Theory. *Int J Multiphase Flow*. 1981;7:167–177.
29. Chahed J, Roig V, Masbernat L. Eulerian–Eulerian two-fluid model for turbulent gas–liquid bubbly flows. *Int J Multiphase Flow*. 2003; 29:23–49.
30. Bellakhel G, Chahed J, Masbernat L. Analysis of the turbulence statistics and anisotropy in homogeneous shear bubbly flow using a turbulent viscosity model. *J Turbulence*. 2004;5:1–16.
31. Augier F, Morchain J, Guiraud P, Masbernat O. Volume fraction gradient-induced flow patterns in a two-liquid phase mixing layer. *Chem Eng Sci*. 2003;58:3985–3993.
32. Kolmogorov AN. On the disintegration of drops in turbulent flow, *Dokl Akad Nauk USSR*. 1949;66:825–828.
33. Hinze J. Fundamentals of the hydrodynamics of splitting dispersion processes. *AIChE J*. 1955;1:289–295.
34. Risso F, Fabre J. Oscillations and breakup of a bubble immersed in a turbulent field. *J Fluid Mech*. 1998;372:323–355.

Manuscript received Jun. 16, 2006, and revision received Oct. 5, 2006.